RSC Advances

PAPER

View Article Online
View Journal | View Issue

Open Access Article. Published on 08 August 2017. Downloaded on 5/1/2025 8:01:24 AM.
This article is licensed under a Creative Commons Attribution 3.0 Unported Licence.

Check for updates

Cite this: *RSC Adv.*, 2017, 7, 38798

First-principles study on the electronic, optical and thermodynamic properties of ABO_3 (A = La,Sr, B = Fe,Co) perovskites

Ting Jia,[a] Zhi Zeng,*[abc] H. Q. Lin,[c] Yuhua Duan[d] and Paul Ohodnicki[d]

Received 12th June 2017
Accepted 19th July 2017

DOI: 10.1039/c7ra06542f

rsc.li/rsc-advances

The electronic, optical and thermodynamic properties of ABO_3 (A = La,Sr, B = Fe,Co) perovskites are investigated using first-principles calculations. The obtained results indicate that $SrCoO_3$ and $SrFeO_3$ are metals, while $LaCoO_3$ and $LaFeO_3$ are insulators and all of them exhibit strong hybridization of the Fe/Co-3d and O-2p orbitals. By correlating the energy band structures with the peaks of the imaginary part of the dielectric function, we obtained the origin of each electron excitation to provide information about the active bands for the corresponding optical transitions observed in the experiment. Moreover, the Debye temperatures θ_D obtained from the phonon frequencies are comparable to the available data. Finally, the thermodynamic properties of the Helmholtz free energy F, entropy S, and constant-volume heat capacity C_v are investigated based on the phonon spectra.

1 Introduction

Perovskites in the form of ABO_3 (A = alkaline-earth metal or La, B = 3d transition metal) are a plentiful family of compounds, which exhibit novel properties, such as colossal magnetoresistance, ferroelectricity and superconductivity, which make them attractive in technological applications such as in catalysis, sensor devices, magnetoresistance devices and spintronics.[1–6] The extensive investigations into ABO_3 not only have technical importance, but also originate from the fundamental interest in the physics of their multiple phases. In the ABO_3 system, the A sites are divalent or trivalent metals, occupied for example by Sr or La atoms. Correspondingly the B sites are tetravalent or trivalent atoms, occupied for example by Co or Fe atoms, resulting in perovskites with desired properties and performances. Usually, the B cations generally determine the physical properties by either the localized or collective behavior of the d electrons. Of course, the valency of the B sites depends on the valency of the A cations, by which the valency of the B transition metal ions change and thus lead to unusual electronic and magnetic properties.

Therefore, the variety of A and B atoms can tailor the structural, electronic, magnetic and other related properties of the perovskites, depending on the size and valence electrons of the A and B atoms. Here, we choose the system of Sr^{2+} and La^{3+} for the A sites, corresponding to Fe/Co^{4+} and Fe/Co^{3+} for the B sites. Both experimental and theoretical studies have been widely carried out on these traditional materials. $SrCoO_3$ has been clarified to be a ferromagnetic metal (T_C = 280 K) with an intermediate-spin d^5 state[7–10] or a high-spin $d^6\underline{L}$ (where $\underline{L}$ denotes a ligand hole) state of Co^{4+}.[11] $SrFeO_3$ is a helical-type antiferromagnet (T_N = 130 K) with a high-spin Fe^{4+} ion.[12,13] Comparatively, there are many more phase transitions in $LaCoO_3$ and $LaFeO_3$. $LaCoO_3$ is a nonmagnetic insulator with low-spin Co^{3+} at low temperatures, but undergoes a transition to a paramagnetic insulator above 90 K and to a paramagnetic metal with high-spin above 500 K.[14–20] The presence of an IS state at 90–500 K (ref. 21) and the structural transition from $R\bar{3}c$ to $R\bar{3}$ at 648 K (ref. 22–24) are controversial. For $LaFeO_3$, a structural transition from *Pbnm* to *R*3*c* has been observed at 1228 K as well as a subsequent transition to *Pm*3*m* at 2140 K.[25] $LaFeO_3$ is a G-type antiferromagnet above T_N = 735 K.[26–28] However, there is little research on the optical and thermodynamic properties.[29–31] Moreover, these data are important both in providing a reference for future research and in improving the range of practical applications. Therefore, in this work, we focus on the ground state at low temperatures to systematically investigate the electronic, optical and thermodynamic properties using first-principles calculations. Our results show that the divalent A sites of $SrCoO_3$ and $SrFeO_3$ are metals, while the trivalent A sites of $LaCoO_3$ and $LaFeO_3$ are insulators, all of which are consistent with experimental results.[8,9,32,33] Based on the electronic structures, their optical and thermodynamic properties are further investigated and summarized to provide a comparison for the experiments.

[a]Key Laboratory of Materials Physics, Institute of Solid State Physics, Chinese Academy of Sciences, Hefei 230031, P. R. China. E-mail: zzeng@theory.issp.ac.cn
[b]Department of Physics, University of Science and Technology of China, Hefei, 230026, P. R. China
[c]Beijing Computational Science Research Center, Beijing 100084, P. R. China
[d]National Energy Technology Laboratory, United States Department of Energy, Pittsburgh, Pennsylvania 15236, USA

 This journal is © The Royal Society of Chemistry 2017

Open Access Article. Published on 08 August 2017. Downloaded on 5/1/2025 8:01:24 AM.
This article is licensed under a Creative Commons Attribution 3.0 Unported Licence.

2 Computational details

Density functional theory (DFT) calculations were performed using the projector-augmented wave (PAW) method[34] implemented in the Vienna *ab initio* simulation package (VASP).[35] The exchange–correlation energy is described by the local spin density approximation (LSDA), or generalized gradient approximation (GGA) using the Perdew–Burke–Ernzerhof (PBE) functional.[36] To account for the strong electron correlation of the Fe and Co ions, all calculations were performed using the Dudarev formalism[37] of the plus Hubbard U correction with $U = 4$ eV, which performs better in describing structures and band gaps with our choice of U values ($U = 4$ and 5 eV). The cutoff energy for the plane-wave basis set is 400 eV, and an $11 \times 11 \times 11$ Monkhorst–Pack k-point mesh[38] for $SrCoO_3$ and $SrFeO_3$, a $5 \times 5 \times 3$ mesh for $LaCoO_3$ and a $6 \times 4 \times 6$ mesh for $LaFeO_3$ were used. All of the shape, volume and ionic coordinates were fully relaxed until the total energy was changed within 10^{-8} eV per atom and the Hellmann–Feynman force on each atomic site is less than 0.0001 eV $Å^{-1}$ for the following phonon calculations.

It is known that all of the optical constants, such as the refractive index n and the extinction coefficient k, can be derived from the dielectric function $\varepsilon = \varepsilon_1(\omega) + i\varepsilon_2(\omega)$. The imaginary part $\varepsilon_2(\omega)$ of the dielectric function is calculated from the momentum matrix elements between the occupied and unoccupied wave functions. The real part $\varepsilon_1(\omega)$ of the dielectric function is evaluated from the imaginary part $\varepsilon_2(\omega)$ by the Kramers–Kronig relationship.[39]

The phonon dispersion and thermodynamic properties were calculated from the harmonic interatomic force constants using the finite displacement method *via* the PHONONPY package.[40] The $2 \times 2 \times 2$ supercell and $5 \times 5 \times 5$ k mesh for $SrCoO_3$ and $SrFeO_3$, the $2 \times 2 \times 1$ supercell and $3 \times 3 \times 3$ k mesh for $LaCoO_3$ and the $2 \times 1 \times 2$ supercell and $3 \times 5 \times 3$ k mesh for $LaFeO_3$ were applied to calculate the force constants.

3 Results and discussion

3.1 Structures

ABO_3 compounds contain a rich family of crystal structures, such as simple cubic, tetragonal, orthorhombic, rhombohedral *etc.* Moreover, the structure of one given ABO_3 compound is complicated due to phase transitions at different temperatures. For example, the structure of $LaFeO_3$ changes from an orthorhombic *Pbnm* phase to rhombohedral $R\bar{3}c$ at 1228 K and subsequently to cubic $Pm\bar{3}m$ at 2140 K.[25] Considering that the properties of the ground state at 0 K are investigated by DFT, we used the crystal structures reported from experiments at low temperatures. $SrCoO_3$ has a perfect perovskite cubic structure with the space group $Pm3m$ [7] (Fig. 1(a)). $SrFeO_3$ has a little distortion to a tetragonal structure with space group $P4/mmm$ [12] (Fig. 1(b)). For compounds with smaller A site ionic radii, the crystal structures of $LaCoO_3$ and $LaFeO_3$ are more distorted to a rhombohedral $R\bar{3}c$ structure[14] (Fig. 1(c)) and an orthorhombic *Pbnm* structure[25] (Fig. 1(d)), respectively. Similarly, the magnetic structures used here are the ground states at low temperatures both from experiment and theory, that are the ferromagnetic structure for $SrCoO_3$,[8–11] the nonmagnetic structure for $LaCoO_3$ (ref. 15, 20 and 29) and the G-type antiferromagnetic structure for $LaFeO_3$.[26–28] For $SrFeO_3$, the ground magnetic state is a non-collinear antiferromagnet with a spiral structure, as shown by experiment.[13] Since the non-collinear magnetic ordering has little influence on the optical and thermodynamic properties, and ferromagnetism has been clarified to be the most stable state among all collinear magnetic phases,[9,41] we selected ferromagnetism as the magnetic structure of $SrFeO_3$ in the following calculations.

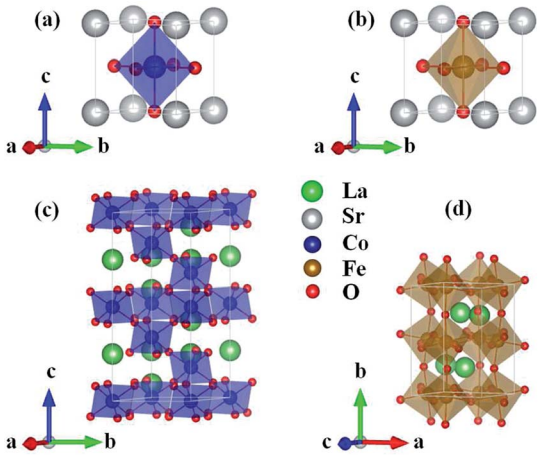

Fig. 1 Crystal structures of the unit cells for (a) $SrCoO_3$, (b) $SrFeO_3$, (c) $LaCoO_3$ and (d) $LaFeO_3$ used in our calculations.

Based on the lattice parameters from the experiment, a full structural optimization was performed using GGA, GGA+U and LSDA+U methods. As shown in Table 1, the lattice constants obtained by GGA+U are much closer to the experimental values than for those obtained by GGA, even for $SrCoO_3$ and $SrFeO_3$ with metal characteristics. Therefore, the correlation U is necessary for the correct prediction of structural information

Table 1 Optimized lattice constants a, b and c (Å) for $SrCoO_3$, $SrFeO_3$, $LaCoO_3$ and $LaFeO_3$ by GGA, GGA+U and LSDA+U methods, compared to the experimental results

Compounds	Methods	a	b	c
$SrCoO_3$	GGA	3.8038	3.8038	3.8038
	GGA+U	3.8174	3.8174	3.8174
	LSDA+U	3.7274	3.7274	3.7274
	Experiment[7]	3.8550	3.8550	3.8550
	GGA	3.8156	3.8156	3.8179
$SrFeO_3$	GGA+U	3.8489	3.8489	3.8513
	LSDA+U	3.7471	3.7471	3.7487
	Experiment[12]	3.8570	3.8570	3.8690
	GGA	5.4440	5.4440	12.8942
$LaCoO_3$	GGA+U	5.4272	5.4272	12.9116
	LSDA+U	5.3119	5.3119	12.6911
	Experiment[14]	5.4427	5.4427	13.0899
	GGA	5.4438	7.6903	5.4758
$LaFeO_3$	GGA+U	5.5607	7.8267	5.5311
	LSDA+U	5.2145	7.5080	5.3292
	Experiment[25]	5.5659	7.8534	5.5544

Open Access Article. Published on 08 August 2017. Downloaded on 5/1/2025 8:01:24 AM.
This article is licensed under a Creative Commons Attribution 3.0 Unported Licence.

and the following properties which are sensitive to the fine structure. In addition, within the LSDA+U method, lattice constants are significantly underestimated compared to those obtained by the GGA+U method and experimentally. Therefore, we selected the most suitable method, GGA+U, for further calculations.

3.2 Electronic properties

The band structures and partial density of states (PDOS) are shown in Fig. 2. The compounds with lower valence A sites, $SrCoO_3$ and $SrFeO_3$, are both metals, which is consistent with experiments and previous calculation results.[8–11,41] The orbitals at the Fermi energy are mainly contributed to by the Fe/Co and O ions. The occupied configurations of d^6L for Co^{4+} and d^5L for Fe^{4+} reflect the strong hybridization of the Fe/Co-3d and O-2p orbitals and are consistent with the negative charge transfer regime of $SrCoO_3$ and $SrFeO_3$ reported before.[8,9,11] These hybridized orbitals give rise to the conduction bands (CBs) and dominate the properties of these oxides, as expected in the case of perovskite oxides. The CBs in the range of 7 to 11 eV are mainly occupied by Sr-4d orbitals. Since Fe^{4+} has one electron less than Co^{4+}, there is little difference at the Fermi level. The minority spin Co-3d states of $SrCoO_3$ are partially occupied and thus cross the Fermi level, reflecting an intermediate-spin state and the metal characteristics of both majority and minority spin. This metal behavior is different from the result of the half metal by the unrestricted Hartree–Fock method,[10] but is similar to the result given by the LSDA+DMFT method.[11] Furthermore, such an intermediate-spin ground state of $SrCoO_3$ has been confirmed by the experimental Co-2p X-ray absorption spectroscopy spectrum, and also the strong hybridization of the d^6L state is key to explain the experimental spectrum.[8,9] Unlike $SrCoO_3$, the minority spin Fe-3d states of $SrFeO_3$ are fully unoccupied, corresponding to the insulating behavior of minority spin and thus the half-metallic property of $SrFeO_3$. Our result of a half-metallic characteristic of ferromagnetic $SrFeO_3$ is slightly different from the metal results from the paramagnetic and antiferromagnetic calculations.[42] In addition, Fe^{4+} is a high-spin state with fully occupied up-spin and unoccupied down-spin Fe-3d orbitals. Considering the charge from the O-2p orbitals, the ground state of Fe^{4+} is a high-spin d^5L configuration, which agrees with the electronic structure of $SrFeO_3$ obtained by X-ray photoemission and ultraviolet photoemission spectroscopy investigations.[43] This negative charge transfer regime is characteristic of compounds with transition metal ions in relatively high oxidation states. The high-valence states of Co^{4+} and Fe^{4+} in $SrCoO_3$ and $SrFeO_3$ correspond to reduced potential energy, which is comparable with or even lower than that of O-2p. As a result, there are charge transfers from O-2p to Fe/Co-3d and thus covalent contributions to the bonding in $SrCoO_3$ and $SrFeO_3$.

While for the compounds with higher valence A sites, $LaCoO_3$ and $LaFeO_3$ with relatively low-valence Co^{3+} and Fe^{3+} cations are more ionic than $SrCoO_3$ and $SrFeO_3$. As shown in Fig. 2, $LaCoO_3$ and $LaFeO_3$ are both insulators, with band gaps of 0.8 and 2.2 eV, which are similar to the experimental results of 0.6 (ref. 32) and 2.1 eV.[33] For $LaCoO_3$, the occupation numbers of the up and down spin states are nearly the same, so the Co^{3+} is the low-spin state and the system is a nonmagnet. The valence bands (VBs) are dominated by the hybridization bands of Co-t_{2g} and O-2p; the lowest CBs are Co-e_g, and the highest CBs are La-4f. The shape and peak locations are similar to existing results.[29] Although the spin-state transition of $LaCoO_3$ at high temperature is controversial, the low-spin ground state at low temperature has reached an agreement by comparing it with the photoemission spectrum.[44] For $LaFeO_3$, since the ground state that we calculated is antiferromagnetic,

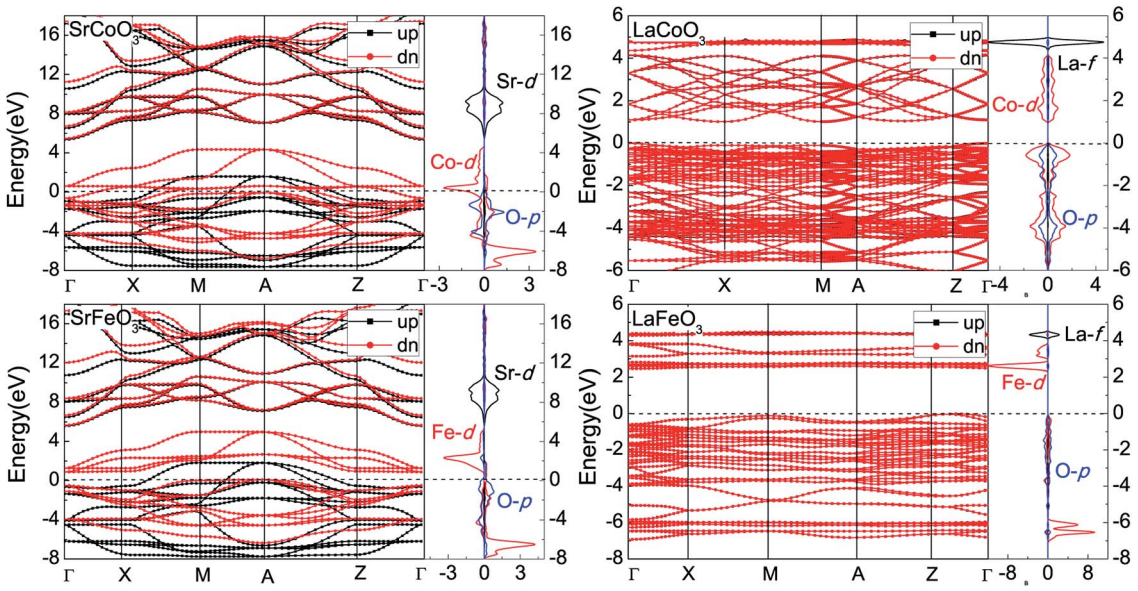

Fig. 2 The band structures and partial density of states for $SrCoO_3$, $SrFeO_3$, $LaCoO_3$ and $LaFeO_3$. The zero of the energy scale is the position of the Fermi level.

Open Access Article. Published on 08 August 2017. Downloaded on 5/1/2025 8:01:24 AM.
This article is licensed under a Creative Commons Attribution 3.0 Unported Licence.

both the up-spin and down-spin states are equal, showing a spin degenerate band structure. However, the PDOS of the up-spin states exhibit spin polarization, especially the Fe-3d orbitals. The up-spin states of the Fe-3d orbitals are fully occupied and down-spin ones are nearly unoccupied, which shows high-spin Fe^{3+} in $LaFeO_3$. There are also hybridization bands of Fe-3d and O-2p near the Fermi level, and the relatively deeper VBs are the fully occupied Fe-3d orbitals. The lowest CBs are the empty Fe-t_{2g} orbitals, which have smaller bandwidths and dispersion than the nearest VBs of Fe-e_g, due to the direct overlap of e_g with O-2p, which is consistent with previous calculation results.[31] The upper narrow and flat CBs in the range of 4.5 to 5 eV are also localized La-4f. Our results are in good agreement with experimental data of the X-ray absorption spectra.[45]

3.3 Optical properties

The optical constants of the dielectric function are shown in Fig. 3. The peaks of the imaginary part of the dielectric function $\varepsilon_2(\omega)$ are related to electron excitation and thus directly connected to the energy band structure. The first peaks of $SrCoO_3$ and $SrFeO_3$ at about 1–2 eV are ascribed to the transitions from the occupied O-2p to the unoccupied Co/Fe-3d or the d–d transition of the Co/Fe-3d states. This peak is very pronounced and higher than the other peaks, which demonstrates that a large number of interband transitions occur at this same energy, corresponding to the concentration of energy bands near the Fermi level. The second peak at about 9 eV is mainly due to the transition from occupied O-2p orbitals to empty Sr-4d orbitals. However, as far as we know no experimental measurements exist for comparison with our theoretical predictions. For $LaCoO_3$ and $LaFeO_3$, the absorptive edges of imaginary part $\varepsilon_2(\omega)$ start at about 0.5 eV and 2.0 eV respectively, relating to the band gaps. In addition, there are relatively more peaks for $LaCoO_3$ and $LaFeO_3$. For $LaCoO_3$, the first two peaks at around 2 eV and 5 eV are attributed to the transitions from the occupied O-2p centered around −0.5 eV and −4 eV below the Fermi level to the empty Co-3d, respectively. These two peaks in the experiment merge to a strong absorption region in the energy region of 1–5 eV.[30] However, the optical properties from the experiment were measured at room temperature so that other spin-states may be mixed, while our calculation results are based on totally low-spin ground states. Therefore, there are some discrepancies. The other peak near 9 eV is contributed to by the transition from the occupied O-2p and Co-3d centered around −4 eV to the empty La-4f near 5 eV. While for $LaFeO_3$, there are only two main peaks below 10 eV. The first one below 5 eV comes from the transition between the occupied O-2p centered around −2 eV and the empty Fe-3d just above 2 eV. The second one between 6 and 10 eV is from multiple transitions: the transition from the occupied O-2p to the empty Fe-3d, the intersite d–d transition between the VB and CB of the Fe-3d centered around −6 and 3 eV, or the transition from the occupied Fe-3d to the CB of La-4f at −4 eV. These two peaks agree well with the experimental results.[31] All of the peaks above 20 eV for $LaCoO_3$ and $LaFeO_3$ correspond to the excitation of the inner electrons to the CB (not shown in the band structures).

Based on the dielectric function, the optical properties, such as the refractive index n and the extinction coefficient k, could be obtained by the equations

$$n = \sqrt{\sqrt{\varepsilon_1(\omega)^2 + \varepsilon_2(\omega)^2} + \varepsilon_1(\omega)} \Big/ \sqrt{2},$$

$$k = \sqrt{\sqrt{\varepsilon_1(\omega)^2 + \varepsilon_2(\omega)^2} - \varepsilon_1(\omega)} \Big/ \sqrt{2}.$$

Our results of n and k as a function of photon wavelength λ are displayed in Fig. 4, both of which oscillate in the short wavelength range. The refractive indices n of $LaCoO_3$ and $LaFeO_3$ increase to a maximum and decay to a static value ($\omega = 0$ or $\lambda \to \infty$) of 3.04 and 2.44, while those of $SrCoO_3$ and $SrFeO_3$ should further increase with increasing λ and finally decay to

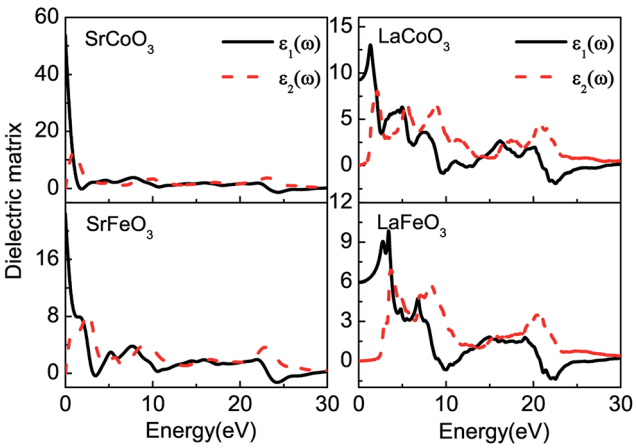

Fig. 3 The real parts $\varepsilon_1(\omega)$ and imaginary parts $\varepsilon_2(\omega)$ of the complex dielectric function for $SrCoO_3$, $SrFeO_3$, $LaCoO_3$ and $LaFeO_3$.

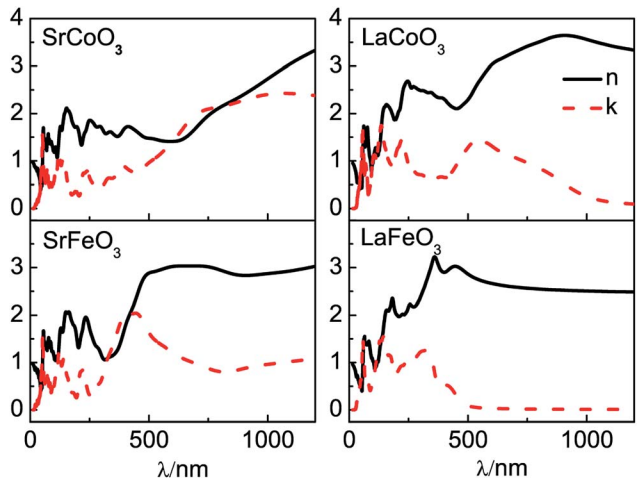

Fig. 4 The optical parameters of the refractive index n and extinction coefficient k for $SrCoO_3$, $SrFeO_3$, $LaCoO_3$ and $LaFeO_3$.

Open Access Article. Published on 08 August 2017. Downloaded on 5/1/2025 8:01:24 AM.
This article is licensed under a Creative Commons Attribution 3.0 Unported Licence.

static values of 7.08 and 4.67 (not shown here). Generally, the static refractive indices of the $SrCoO_3$ and $SrFeO_3$ metals are relatively larger than those of the $LaCoO_3$ and $LaFeO_3$ insulators. Since the refractive index n and extinction coefficient k are directly proportional to real part $\varepsilon_1(\omega)$ and the imaginary $\varepsilon_2(\omega)$ of the dielectric function, both of them are directly connected to the energy band structure and they are equivalent in describing the optical properties. The extinction coefficient k is similar to the imaginary part of the dielectric function $\varepsilon_2(\omega)$, which is directly related to electron excitation. The peaks of k directly correspond to those of $\varepsilon_2(\omega)$ we analyzed above, but the wavelength dependence of the extinction coefficient k is shown here. The values of k go down to 0 at about 1000 nm and 500 nm for $LaCoO_3$ and $LaFeO_3$, respectively. These optical gaps are due to their insulating behavior, which is absent for $SrCoO_3$ and $SrFeO_3$. The refractive index n and extinction coefficient k provided here are used for experimental comparison.

3.4 Thermodynamic properties

To obtain the temperature dependence of the thermodynamic parameters, the phonon spectrum was firstly calculated using a finite displacement method. As shown in Fig. 5, there are no imaginary phonon modes for all of these compounds, indicating their dynamical stability. Since the wave number is proportional to the number of atoms, there are 15, 90 and 60 phonon bands for $SrCoO_3$($SrFeO_3$), $LaCoO_3$ and $LaFeO_3$ with 5, 30 and 20 atoms per unit cell, respectively. Besides, the phonon PDOS that are presented in Fig. 5 match the phonon dispersion. The flat regions of the phonon-dispersion curves, which correspond to the peaks in the phonon PDOS, indicate the localization of the states. These phonon spectra can be divided into three parts: (1) the low frequency modes of the acoustic phonon branches below about 4 THz are mainly contributed to by La/Sr atoms together with slight contributions from other atoms. (2) The middle frequency range of the optical branches are mixed Fe/Co–O modes (4–12 THz for $SrCoO_3$ and $SrFeO_3$, and 4–16 THz for $LaCoO_3$ and $LaFeO_3$). (3) The high frequency mode optical branches are nearly always contributed by O atoms. This is consistent with the fact that other atoms are much heavier than O atoms, as frequency is inversely proportional to atomic mass. In addition, the maximum values of the vibrational frequency for $LaCoO_3$ and $LaFeO_3$ are larger than those for $SrCoO_3$ and $SrFeO_3$. This suggests a stronger bonding in $LaCoO_3$ and $LaFeO_3$.

The Debye temperature θ_D is an important parameter for the thermophysical properties of materials. This fundamental parameter is useful for the analysis of the specific heat, thermal conductivity and melting temperature. The Debye temperature is not a strictly determined parameter, but is obtained through well established empirical or semiempirical formulae. Here, we calculated it from the highest frequency of the normal mode vibration (Debye frequency) ω_m,

$$\theta_D = \hbar\omega_m n^{1/3}/k_B,$$

where $\hbar$ is the reduced Planck constant, k_B is the Boltzmann constant and n is the number of atoms per unit cell. $n^{1/3}$ is used to correct the error caused by the reduction of the Brillouin zone and thus cutting off the phonon frequencies at smaller values.[46] Because the size of the unit cell in real space increases with increasing n, the Brillouin zone boundary moves inward. When the highest frequency of the normal mode vibration $\omega_m = 4.10$, 4.53, 2.56 and 2.73 THz, and there are 5, 5, 30 and 20 atoms per unit cell for $SrCoO_3$, $SrFeO_3$, $LaCoO_3$ and $LaFeO_3$, the Debye temperatures could be obtained at 335.58, 371.37, 381.79 and 355.67 K, respectively. Our results are comparable to the available data: θ_D is 353 K for $SrCoO_3$ from a previous experiment,[47] 286 K for $SrFeO_3$ calculated from the elastic constants[48] and 480 and 407 K for $LaCoO_3$ (ref. 49) and $LaFeO_3$ (ref. 27) from previous experiments.

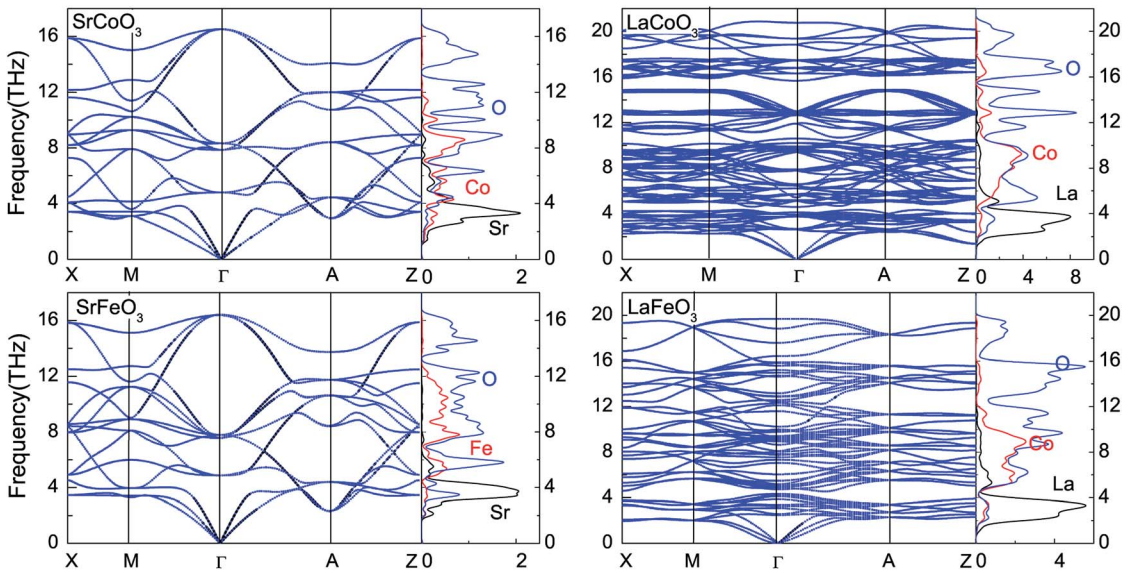

Fig. 5 Phonon dispersion curves and partial density of states for $SrCoO_3$, $SrFeO_3$, $LaCoO_3$ and $LaFeO_3$.

Open Access Article. Published on 08 August 2017. Downloaded on 5/1/2025 8:01:24 AM.
This article is licensed under a Creative Commons Attribution 3.0 Unported Licence.

Furthermore, the thermodynamic functions can be obtained by the phonon spectrum, assuming that the lattice vibrational degrees of freedom play a more noticeable role than the electronic degrees of freedom. As shown in Fig. 6, the temperature dependence of the Helmholtz free energy F, entropy S, and constant-volume heat capacity C_v are calculated within the harmonic approximation. With an increase in temperature, the free energy decreases, while both the entropy and heat capacity increase from zero at 0 K, all of which conform to the third law of thermodynamics. Moreover, at low temperatures that are much lower than the Debye temperatures, the constant-volume heat capacity C_v is proportional to temperature T^3. The contribution of the lattice heat capacity at low temperatures is mainly from the long wavelength vibration modes of the lattice, which could be approximated by treating the lattice as a continuum. However, at high temperatures, C_v tends to the Dulong–Petit classical limit which is proportional to the number of atoms per unit cell.

4 Conclusions

In summary, the electronic, optical and thermodynamic properties of ABO_3 (A = La,Sr and B = Fe,Co) perovskites are investigated using first-principles calculations. The structural parameters we optimized and the energy gaps we obtained by the GGA+U method are in good agreement with the experimental data. The strong hybridization of the Fe/Co-3d and O-2p orbitals dominates the properties of these oxides, which is a common characteristic for perovskite oxides. Based on the electronic structure, the dielectric function, refractive index and extinction coefficient are obtained and discussed. The static refractive indices of $SrCoO_3$ and $SrFeO_3$ are relatively larger than those of $LaCoO_3$ and $LaFeO_3$. Furthermore, based on the phonon frequencies, we obtained Debye temperatures θ_D that are comparable to the available data. Finally, by using the calculated phonon dispersion, the thermodynamic properties of the Helmholtz free energy, entropy, and constant-volume heat capacity are obtained within the harmonic approximation, all of which conform to the third law of thermodynamics. Finally, ABO_3 perovskites are flexible systems as their properties can be adjusted or enhanced for specific applications by chemical doping at the A or B cation sites. Therefore, the doped (La,Sr)(Fe,Co)O_3 compounds will be investigated to improve the performance of the pure parent materials in our further work.

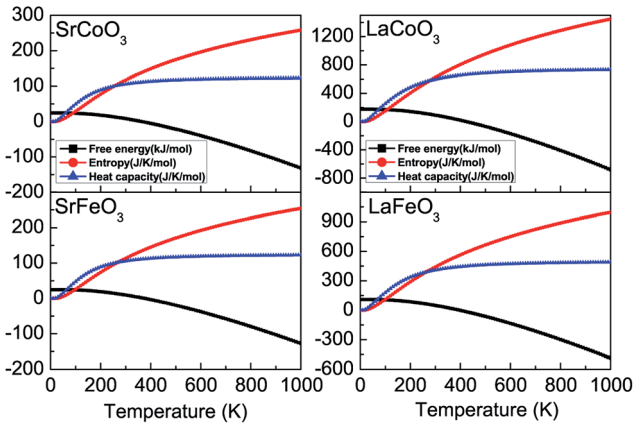

Fig. 6 The thermodynamic parameters of free energy, entropy, and constant volume heat capacity for $SrCoO_3$, $SrFeO_3$, $LaCoO_3$ and $LaFeO_3$.

Acknowledgements

This work was supported by the National Science Foundation of China under Grant No. 11534012, and U1230202 (NSAF), the special Funds for Major State Basic Research Project of China (973) under Grant No. 2012CB933702 and the Director Grants of CASHIPS. The calculations were partly performed in the Center for Computational Science of CASHIPS, the ScGrid of the Supercomputing Center and the Computer Network Information Center of the Chinese Academy of Sciences, and partly using the Tianhe-2JK computing time award at the Beijing Computational Science Research Center (CSRC).

References

1 J. Suntivich, K. J. May, H. A. Gasteiger, J. B. Goodenough and Y. Shao-Horn, *Science*, 2011, **334**, 1383–1385.
2 A. J. Millis, *Nature*, 1998, **392**, 147–150.
3 T. Arakawa, H. Kurachi and J. Shiokawa, *J. Mater. Sci.*, 1985, **20**, 1207–1210.
4 A. A. Bokov and Z.-G. Ye, *J. Mater. Sci.*, 2006, **41**, 31–52.
5 A. M. Schultz, T. D. Brown, M. P. Buric, S. Lee, K. Gerdes and P. R. Ohodnicki, *Sens. Actuators, B*, 2015, **221**, 1307–1313.
6 A. M. Schultz, T. D. Brown and P. R. Ohodnicki, *J. Phys. Chem. C*, 2015, **119**, 6211–6220.
7 Y. Wang, L. Yu, J. Wang, L. Chen, W. Gao, X. Du and L. Biao, *Mater. Lett.*, 2012, **75**, 39–41.
8 R. H. Potze, G. A. Sawatzky and M. Abbate, *Phys. Rev. B: Condens. Matter Mater. Phys.*, 1995, **51**, 11501–11506.
9 M. Abbate, G. Zampieri, J. Okamoto, A. Fujimori, S. Kawasaki and M. Takano, *Phys. Rev. B: Condens. Matter Mater. Phys.*, 2002, **65**, 165120.
10 M. Zhuang, W. Zhang, A. Hu and N. Ming, *Phys. Rev. B: Condens. Matter Mater. Phys.*, 1998, **57**, 13655–13659.
11 J. Kuneš, V. Křápek, N. Parragh, G. Sangiovanni, A. Toschi and A. V. Kozhevnikov, *Phys. Rev. Lett.*, 2012, **109**, 117206.
12 S. Diodati, L. Nodari, M. M. Natile, U. Russo, E. Tondello, L. Lutterotti and S. Gross, *Dalton Trans.*, 2012, **41**, 5517.
13 T. Takeda, Y. Yamaguchi and H. Watanabe, *J. Phys. Soc. Jpn.*, 1972, **33**, 967–969.
14 C. Autret, J. Hejtmánek, K. Knížek, M. Maryško, Z. Jirák, M. Dlouhá and S. Vratislav, *J. Phys.: Condens. Matter*, 2005, **17**, 1601–1616.
15 M. Señarís-Rodríguez and J. Goodenough, *J. Solid State Chem.*, 1995, **116**, 224–231.
16 P. G. Radaelli and S.-W. Cheong, *Phys. Rev. B: Condens. Matter Mater. Phys.*, 2002, **66**, 094408.
17 K. Asai, A. Yoneda, O. Yokokura, J. M. Tranquada, G. Shirane and K. Kohn, *J. Phys. Soc. Jpn.*, 1998, **67**, 290–296.

Open Access Article. Published on 08 August 2017. Downloaded on 5/1/2025 8:01:24 AM.
This article is licensed under a Creative Commons Attribution 3.0 Unported Licence.

18 M. W. Haverkort, Z. Hu, J. C. Cezar, T. Burnus, H. Hartmann, M. Reuther, C. Zobel, T. Lorenz, A. Tanaka, N. B. Brookes, H. H. Hsieh, H.-J. Lin, C. T. Chen and L. H. Tjeng, *Phys. Rev. Lett.*, 2006, **97**, 176405.
19 A. Podlesnyak, S. Streule, J. Mesot, M. Medarde, E. Pomjakushina, K. Conder, A. Tanaka, M. W. Haverkort and D. I. Khomskii, *Phys. Rev. Lett.*, 2006, **97**, 247208.
20 T. Saitoh, T. Mizokawa, A. Fujimori, M. Abbate, Y. Takeda and M. Takano, *Phys. Rev. B: Condens. Matter Mater. Phys.*, 1997, **55**, 4257–4266.
21 M. A. Korotin, S. Y. Ezhov, I. V. Solovyev, V. I. Anisimov, D. I. Khomskii and G. A. Sawatzky, *Phys. Rev. B: Condens. Matter Mater. Phys.*, 1996, **54**, 5309–5316.
22 J. B. Goodenough and P. M. Raccah, *J. Appl. Phys.*, 1965, **36**, 1031–1032.
23 P. M. Raccah and J. B. Goodenough, *Phys. Rev.*, 1967, **155**, 932–943.
24 G. Thornton, B. Tofield and A. Hewat, *J. Solid State Chem.*, 1986, **61**, 301–307.
25 S. M. Selbach, J. R. Tolchard, A. Fossdal and T. Grande, *J. Solid State Chem.*, 2012, **196**, 249–254.
26 S. Stølen, F. Grønvold, H. Brinks, T. Atake and H. Mori, *J. Chem. Thermodyn.*, 1998, **30**, 365–377.
27 S. Parida, S. Rakshit and Z. Singh, *J. Solid State Chem.*, 2008, **181**, 101–121.
28 D. D. Sarma, N. Shanthi, S. R. Barman, N. Hamada, H. Sawada and K. Terakura, *Phys. Rev. Lett.*, 1995, **75**, 1126–1129.
29 A. Laref and S. Jun Luo, *J. Phys. Soc. Jpn.*, 2010, **79**, 064702.
30 L. V. Nomerovannaya, A. A. Makhnev, S. V. Streltsov, I. A. Nekrasov, M. A. Korotin, S. V. Shiryaev, G. L. Bychkov, S. N. Barilo and V. I. Anisimov, *J. Phys.: Condens. Matter*, 2004, **16**, 5129–5136.
31 M. D. Scafetta, A. M. Cordi, J. M. Rondinelli and S. J. May, *J. Phys.: Condens. Matter*, 2014, **26**, 505502.
32 A. Chainani, M. Mathew and D. D. Sarma, *Phys. Rev. B: Condens. Matter Mater. Phys.*, 1992, **46**, 9976–9983.
33 T. Arima, Y. Tokura and J. B. Torrance, *Phys. Rev. B: Condens. Matter Mater. Phys.*, 1993, **48**, 17006–17009.
34 P. E. Blöchl, *Phys. Rev. B: Condens. Matter Mater. Phys.*, 1994, **50**, 17953–17979.
35 G. Kresse and J. Furthmüller, *Comput. Mater. Sci.*, 1996, **6**, 15–50.
36 J. P. Perdew, K. Burke and M. Ernzerhof, *Phys. Rev. Lett.*, 1996, **77**, 3865–3868.
37 S. L. Dudarev, G. A. Botton, S. Y. Savrasov, C. J. Humphreys and A. P. Sutton, *Phys. Rev. B: Condens. Matter Mater. Phys.*, 1998, **57**, 1505–1509.
38 H. J. Monkhorst and J. D. Pack, *Phys. Rev. B: Solid State*, 1976, **13**, 5188–5192.
39 M. Gajdoš, K. Hummer, G. Kresse, J. Furthmüller and F. Bechstedt, *Phys. Rev. B: Condens. Matter Mater. Phys.*, 2006, **73**, 045112.
40 A. Togo, F. Oba and I. Tanaka, *Phys. Rev. B: Condens. Matter Mater. Phys.*, 2008, **78**, 134106.
41 I. R. Shein, *Phys. Solid State*, 2005, **47**, 2082.
42 S. Mathi Jaya, R. Jagadish, R. S. Rao and R. Asokamani, *Phys. Rev. B: Condens. Matter Mater. Phys.*, 1991, **43**, 13274–13279.
43 A. E. Bocquet, A. Fujimori, T. Mizokawa, T. Saitoh, H. Namatame, S. Suga, N. Kimizuka, Y. Takeda and M. Takano, *Phys. Rev. B: Condens. Matter Mater. Phys.*, 1992, **45**, 1561–1570.
44 M. Abbate, R. Potze, G. A. Sawatzky and A. Fujimori, *Phys. Rev. B: Condens. Matter Mater. Phys.*, 1994, **49**, 7210–7218.
45 Z. Y. Wu, M. Benfatto, M. Pedio, R. Cimino, S. Mobilio, S. R. Barman, K. Maiti and D. D. Sarma, *Phys. Rev. B: Condens. Matter Mater. Phys.*, 1997, **56**, 2228–2233.
46 D. T. Morelli and G. A. Slack, in *High Thermal Conductivity Materials*, Springer-Verlag, New York, 2006, pp. 37–68.
47 S. Balamurugan, K. Yamaura, A. B. Karki, D. P. Young, M. Arai and E. Takayama-Muromachi, *Phys. Rev. B: Condens. Matter Mater. Phys.*, 2006, **74**, 172406.
48 H. Rached, D. Rached, M. Rabah, R. Khenata and A. H. Reshak, *Phys. B*, 2010, **405**, 3515–3519.
49 C. He, H. Zheng, J. F. Mitchell, M. L. Foo, R. J. Cava and C. Leighton, *Appl. Phys. Lett.*, 2009, **94**, 102514.

 This journal is © The Royal Society of Chemistry 2017